Geophysical Research Letters

RESEARCH LETTER
10.1029/2026GL121981

Calcium Solubility of Bridgmanite in Subducted Basalt in Earth's Lower Mantle

Chengwei Zhang[1], Takashi Yoshino[2], Elias El Ghazaoui[3], Stella Chariton[4], Vitali B. Prakapenka[4], Luo Li[1], Yanyao Zhang[5], and Jung-Fu Lin[1]

[1]Department of Earth and Planetary Sciences, Jackson School of Geosciences, The University of Texas at Austin, Austin, TX, USA, [2]Institute for Planetary Materials, Okayama University, Misasa, Japan, [3]School of Earth and Environmental Sciences, Seoul National University, Seoul, Korea, [4]Center for Advanced Radiation Sources, The University of Chicago, Chicago, IL, USA, [5]Earth and Planetary Sciences, Stanford University, Stanford, CA, USA

Key Points:

- Calcium solubility of bridgmanite in a basaltic composition was investigated experimentally up to 125 GPa and 3,520 K
- Thermodynamic modeling of the solvus shows limited Ca solubility of 0.001–0.03 cations in bridgmanite at lower-mantle conditions
- Davemaoite is estimated to account for 8 and 25 vol% in pyrolite and subducted basalt assemblages, respectively, along mantle geotherms

Supporting Information:

Supporting Information may be found in the online version of this article.

Correspondence to:

J.-F. Lin,
afu@jsg.utexas.edu

Citation:

Zhang, C., Yoshino, T., El Ghazaoui, E., Chariton, S., Prakapenka, V. B., Li, L., et al. (2026). Calcium solubility of bridgmanite in subducted basalt in Earth's lower mantle. *Geophysical Research Letters*, *53*, e2026GL121981. https://doi.org/10.1029/2026GL121981

Received 20 JAN 2026
Accepted 25 JUN 2026

Abstract The calcium solubility in bridgmanite and the resulting abundance of davemaoite under lower-mantle pressure-temperature conditions have been under debate following a recent report of extensive calcium dissolution in bridgmanite. We experimentally investigated the calcium solubility in bridgmanite in a basaltic composition at pressures up to 125 GPa and temperatures up to 3,520 K. Our experimental data are modeled thermodynamically along the bridgmanite-davemaoite solvus to quantify the calcium solubility in bridgmanite and the davemaoite proportion in basaltic and pyrolitic assemblages along lower mantle geotherms. Our results indicate that bridgmanite hosts only 0.001–0.03 Ca cations per formula unit in the lower mantle, while davemaoite remains as an abundant mineral, accounting for 8 and 25 vol% of pyrolitic and basaltic mineralogical models, respectively, along representative lower-mantle geotherms. Our thermoelastic modeling further indicates that the effect of calcium dissolution on the density and bulk sound velocity of lower-mantle assemblages is negligible.

Plain Language Summary Bridgmanite and davemaoite are considered the first and third most abundant minerals in Earth's lower mantle, respectively. Davemaoite ($CaSiO_3$) can dissolve into bridgmanite (Fe, Al-bearing $MgSiO_3$) at extremely high-pressure and high-temperature conditions of the lower mantle, but the extent of this dissolution and the amount of davemaoite that remains are still a hotly contested topic. We performed high pressure-temperature X-ray diffraction experiments, quenched sample chemical and structural analyses, and thermodynamic modeling to determine how much calcium dissolves into bridgmanite and how this process changes the mineralogical composition of a subducted basalt at lower mantle conditions. Our results show that bridgmanite contains only a very small amount of calcium and that this dissolution only slightly reduces the proportion of davemaoite in current mineralogical models of the lower mantle. We also examined how calcium dissolution into bridgmanite affects the physical properties of lower-mantle assemblages and found that its influence on density and seismic wave speeds is minor.

1. Introduction

Bridgmanite (Bgm; Fe, Ca, Al-bearing $MgSiO_3$) is the most abundant mineral of the lower mantle, while davemaoite (Dvm; $CaSiO_3$) is proposed to be the third most abundant mineral of the region in most mineralogical models. Their distributions in the lower mantle differ among proposed rock assemblages. For example, a classic pyrolitic compositional model indicates 75 vol% Bgm and 8 vol% Dvm contents in the lower mantle (Irifune et al., 2010; Ishii et al., 2018; Kesson et al., 1998; Ricolleau et al., 2009), whereas subducted basaltic composition would contain approximately 27 vol% Bgm and 25 vol% Dvm (Ishii et al., 2019, 2022; Ricolleau et al., 2010). The relative Bgm and Dvm abundances have important ramifications for lower-mantle composition, seismology, and geodynamics because they display distinct elastic and rheological properties (Immoor et al., 2022; Zhou et al., 2025).

Bgm can accommodate a certain amount of calcium (Ca), but the extent of Dvm dissolution in Bgm and the maximum amount of Ca that Bgm can incorporate remain under debate. Recent diamond-anvil cell (DAC) experiments suggest that Dvm can substantially dissolve into Bgm, forming Ca-rich bridgmanite (Ca-Bgm) at high pressure-temperature (P-T) conditions (40–110 GPa and 2,300–3,000 K), with Ca solubility (χ_{Ca}) as high as 0.20 cations per formula unit (Ko et al., 2022). This interpretation is based primarily on the disappearance of Dvm peaks in situ X-ray diffraction (XRD) patterns at high P-T conditions and post-quench high-resolution

transmission electron microscopy (HRTEM) analyses of the recovered samples. It implies that Dvm could largely disappear in the deeper lower mantle, forming a "one-perovskite domain." Such extensive Dvm dissolution is also supported by density functional theory calculations, which predict that Fe-bearing Bgm can enhance Ca dissolution, whereas Al may suppress it (Muir et al., 2021; Muir & Zhang, 2022). These findings challenge conventional lower-mantle mineralogical models and could influence geodynamic models and interpretations of seismic observations (Ko et al., 2022; Zhou et al., 2025).

Recent multi-anvil press (MAP) experiments suggested that the high χ_{Ca} in Bgm reported in previous DAC experiments may reflect kinetic effects associated with metastable Ca-Bgm formation and nm-sized grains (Wang et al., 2025). The small grain sizes of the quenched samples may complicate post-quench HRTEM analyses, potentially causing neighboring Bgm and Dvm grains to contaminate each other's measured compositions. The MAP experiments produced large grains and reported much lower χ_{Ca} in Bgm, less than 0.021 cations per formula unit at 27–50 GPa and 2,300–2,700 K, approximately one order of magnitude lower than those reported in DAC experiments (Wang et al., 2025). However, these experiments did not use in situ XRD to observe phase formation at high P-T conditions and were limited to pressures below 50 GPa. Thus, whether Dvm dissolution into Bgm increases in the deeper lower mantle remains unresolved. In addition, a thermodynamic framework is still needed to fundamentally and quantitatively evaluate how χ_{Ca} and the coexisting Dvm proportion vary with relevant lower-mantle P-T and compositional conditions.

Earth's lower mantle can contain several mineralogical assemblages ranging from pyrolite to subducted basalt (McDonough & Sun, 1995; A. E. Ringwood, 1991). Subducted mid-ocean ridge basalt (MORB) along ancient subduction zones is considered a source of heterogeneities in Earth's lower mantle due to its distinct composition relative to the surrounding pyrolitic mantle. Subducted MORB has notably more CaO and Al_2O_3, but less MgO (A. Ringwood and Irifune, 1988). Under lower-mantle conditions, MORB is composed of Bgm, Dvm, stishovite (St), and a Ca-ferrite-type aluminous phase (CF), with proportions of approximately 25–30, 23–27, 19–23, and 24–28 vol% for these phases, respectively (Ishii et al., 2019, 2022; Ricolleau et al., 2010). High P-T DAC experiments on MORB compositions using crystalline starting materials can help constrain Dvm dissolution into Bgm at relevant lower-mantle conditions because the relatively high abundances of both Dvm and Bgm make them more readily detectable in XRD patterns and more suitable for HRTEM analysis. Thermodynamic modeling of high P-T phase relations in subducted MORB under lower-mantle conditions can further help constrain the origin of lower-mantle heterogeneities.

In this study, the dissolution of Dvm into Bgm in a representative basaltic composition was examined at 33–125 GPa and 1,581–3,520 K using double-sided laser-heated DAC experiments coupled with in situ synchrotron XRD. Crystalline and glassy starting materials were used to help address the aforementioned high P-T, compositional, and kinetic effects. The quenched samples were further analyzed by HRTEM to determine phase assemblages and compositions. A thermodynamic model of the Bgm-Dvm solvus was developed to calculate the Ca content in Bgm and Dvm proportions along representative lower-mantle geotherms. We further used thermoelastic calculations to evaluate how the Ca dissolution and the resulting changes in Dvm abundance affect density and seismic velocities in pyrolite and MORB at lower-mantle conditions. Our study provides new constraints on the Ca solubility in Bgm, Dvm stability, and the seismic velocity contrasts between MORB and the surrounding mantle.

2. Materials and Methods

2.1. Starting Material

Crystalline and glassy starting materials with similar bulk compositions were synthesized to evaluate starting-material-dependent kinetic effects on Dvm dissolution into Bgm. The composition was designed to contain approximately equal proportions of Bgm and Dvm using phase compositions reported for subducted basalt (Ishii et al., 2022; Ricolleau et al., 2010). The precursor silicate glass was synthesized from FeO, MgO, Al_2O_3, SiO_2, and $CaCO_3$ powders by drying, stepwise heating to 1,073 and 1,873 K, and quenching. The crystalline starting material was synthesized by recrystallizing the precursor glass at 24 GPa and 2,073 K for 1 min to produce grains smaller than the laser-heating spot size used in subsequent laser-heated DAC experiments. Its measured bulk composition is 47.9 mol% SiO_2, 19.4 mol% CaO, 16.2 mol% MgO, 10.8 mol% FeO, and 5.7 mol% Al_2O_3, similar to that of the glassy starting material, which contains 47.1 mol% SiO_2, 18.3 mol% CaO, 16.8 mol% MgO,

12.1 mol% FeO, and 5.7 mol% Al_2O_3. Similar bulk compositions allow direct comparison of starting-material-dependent kinetic effects on phase formation during laser heating, while detailed synthesis and preparation procedures are described in Text S1 in Supporting Information S1.

2.2. In Situ X-Ray Diffraction With Laser-Heated DAC Experiments

High P-T laser-heated DAC experiments coupled with in situ XRD were conducted at the 13IDD station at the GSECARS of the Advanced Photon Source, Argonne National Laboratory (Prakapenka et al., 2008). In situ XRD patterns were collected by an Eiger2 CdTe 9M detector, and the monochromatic incident X-ray beam had a wavelength of 0.3344 Å. The laser beams with a diameter of 15 μm on both sides of the sample were aligned coaxially with the X-ray focused to a beam size of ~1.5 × 1.5 μm^2 (full width at half maximum, FWHM). One to four non-overlapping ~15 μm-diameter heating spots on each sample were heated for 1–7 min. During heating, diffraction patterns were continuously collected with 5–10 s exposures, followed by rapid quenching to preserve high-T assemblages. After quenching, XRD patterns were also collected by rotating the sample stage over $\omega = \pm 5^{\circ}$ during a 20 s exposure period. The XRD patterns were refined using Rietveld and Le Bail methods to identify phase assemblages and unit-cell parameters, with detailed heating and analysis procedures provided in Text S2 in Supporting Information S1.

2.3. Chemical Analysis of the Quenched Samples

Recovered samples were milled using a focused ion beam (FIB; Scios 2 HiVac DualBeam) to prepare lamellae for further HRTEM analysis at the Texas Materials Institute, University of Texas at Austin. The sub-angstrom electron probe (~0.08 nm) and atomic spatial resolution (0.078 nm) enabled nanoscale chemical analysis, although the effective analytical spatial resolution of HRTEM–EDS depends on the interaction volume within the ~100 nm-thick FIB lamellae. Nano-beam electron diffraction was used to confirm the quenched phases. Ferric iron ratios in Bgm were determined by electron energy-loss spectroscopy following van Aken and Liebscher (2002). Phase proportions were estimated by mass-balance calculations. Additional details on FIB preparation and HRTEM analysis are provided in Text S3 in Supporting Information S1.

3. Results and Discussion

3.1. Phases Present at High P-T

To evaluate whether the apparent disappearance of Dvm XRD peaks reflects true Dvm dissolution into Bgm or starting-material-dependent kinetic effects, we compared in situ XRD patterns from crystalline and glassy starting materials over 33–125 GPa and 1,581–3,520 K. In situ XRD patterns collected from crystalline starting materials show sharp and well-resolved diffraction peaks, allowing reliable phase identification and Rietveld refinement (Figure 1, Figures S1 and S2 in Supporting Information S1). Rietveld refinements show that the crystalline-derived samples contain 55.4–58.2 vol% Bgm (space group *Pbnm*), 41.4–43.9 vol% Dvm (space group $Pm\bar{3}m$), and 0.4–0.8 vol% St (space group $P4_2/mnm$). At higher pressures (~68 GPa), St transformed to $CaCl_2$–type SiO_2 (space group *Pnnm*) (Sun et al., 2019). In contrast, runs using the glassy starting material show broader XRD peaks with larger FWHM, stronger peak overlap, and lower intensities (Figure 1b), consistent with finer-grained quenched products (Figure 2b). The FWHM values are ~2–6-fold higher for Bgm and ~1.2–1.5-fold higher for Dvm in the glass-derived runs than in the crystalline-derived runs (Figure S2 in Supporting Information S1). For selected glass-derived runs, extending the heating duration to 300–420 s did not noticeably improve the XRD pattern quality (Figure S3 in Supporting Information S1). Consequently, the glass-derived XRD patterns were analyzed using Le Bail rather than Rietveld refinements. Phase proportions for the glass-derived runs were therefore determined from complementary HRTEM results. The weak, broadened, and overlapping Dvm peaks can give the appearance that Dvm has disappeared from the diffraction patterns (Figure 1b). Similar observations in previous DAC studies were interpreted as complete Dvm dissolution into Bgm (Ko et al., 2022). However, the strong contrast in Dvm peak intensity and peak width between the crystalline and glass starting-material experiments suggests that the weak Dvm signals in the glass runs are primarily a consequence of kinetic effects—specifically, the formation of numerous nm-sized Dvm grains—rather than complete dissolution of Dvm into Bgm (see HRTEM analysis for further discussion).

Lattice parameters and equation of state (EOS) results of Bgm were obtained from our XRD data and used to compare its unit-cell volume with previously reported bridgmanite compositions (Figure S4 in Supporting

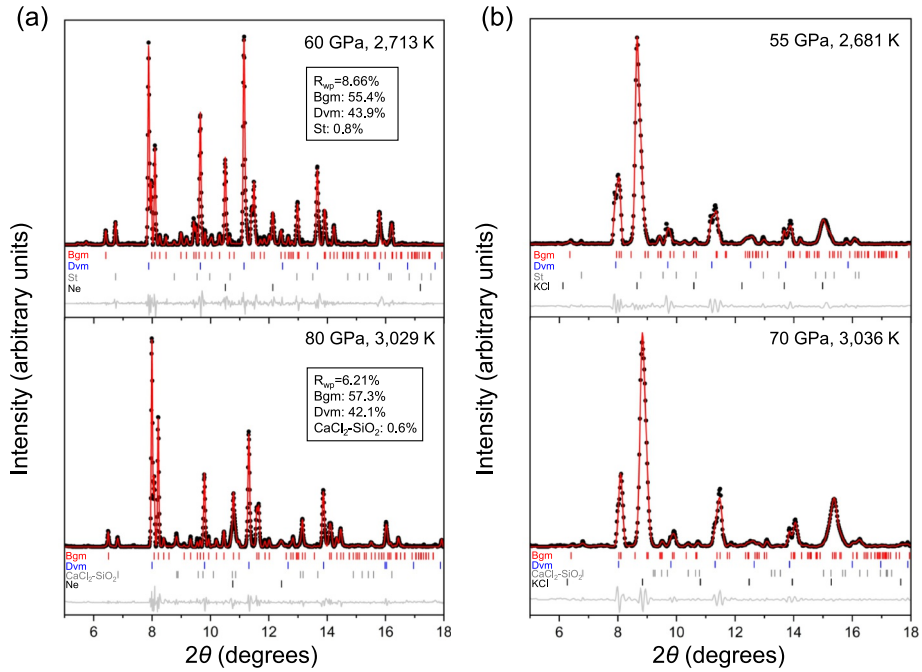

Figure 1. X-ray diffraction refinements of high-pressure and high-temperature run products. (a) Refinement by the Rietveld method using the crystalline starting sample; (b) refinement by the Le Bail method using the glassy starting sample. The Le Bail method was used for refinement in (b) because of broad diffraction peaks and relatively poor diffraction quality. Observed intensities are in black dots; calculated profiles are in red curves; residuals are shown in gray. Vertical colored ticks denote peak positions for each identified phase: bridgmanite (red), davemaoite (blue), stishovite or $CaCl_2$–type SiO_2 (gray), and KCl or Ne pressure medium (black). Panel legends show the residual factor (Rwp) together with the volume proportions of the identified phases derived from Rietveld refinements. The wavelength of the incident X-ray beam is 0.3344 Å.

Information S1). The volume data, consisting of 14 P–V data points collected after annealing at each pressure, were fitted with a second-order Birch–Murnaghan EOS with a fixed pressure derivative ($K_{\prime}^{0} = 4$). The fitted parameters are $V_0 = 169.4 \pm 0.4$ Å^3 and $K_0 = 242 \pm 4$ GPa. The covariance matrix of the fitted parameters $[V_0, K_0]$ is $\begin{bmatrix} 0.16 & -1.60 \\ -1.60 & 17.31 \end{bmatrix}$. Our Bgm has Fe–Al-rich compositions (e.g., $Ca_{0.02}Mg_{0.60}Fe_{0.34}Al_{0.25}Si_{0.79}O_3$) and shows unit-cell volumes consistent with previously reported Fe–Al-rich Bgm compositions (e.g., $Ca_{0.01}Mg_{0.54}Na_{0.02}Fe_{0.36}Al_{0.33}Ti_{0.05}Si_{0.69}O_3$) (Ishii et al., 2022; Ricolleau et al., 2010). These Fe–Al-rich Bgm compositions have larger unit-cell volumes than Fe-Al-poor Bgm ($Mg_{0.88}Fe_{0.13}Al_{0.11}Si_{0.88}O_3$) and $MgSiO_3$ perovskite (Pv) (Catalli et al., 2011; Tange et al., 2012). The unit-cell volume of the reported "Ca-Bgm" (e.g., $Ca_{0.17}Mg_{0.59}Fe_{0.19}Al_{0.15}Si_{0.9}O_3$) from Ko et al. (2022) is also comparable to that of Fe–Al–rich Bgm. Thus, a larger unit-cell volume of Bgm is not, by itself, a robust indicator of high Ca contents, as previous studies have shown that Fe and Al substitutions also increase the unit-cell volume (Andrault et al., 2001; Criniti et al., 2024; Wolf et al., 2015).

3.2. Calcium Solubility in Bridgmanite at Lower Mantle Conditions

HRTEM analyses were conducted to test whether weak Dvm XRD signals in the glass-derived runs reflect true Dvm disappearance and to determine phase compositions in the quenched samples. High-angle annular dark-field images and energy-dispersive X-ray spectroscopy (EDS) chemical mapping of the recovered samples show that three phases are present in the quenched assemblages: Bgm, St ($CaCl_2$–type SiO_2 at pressures above ~68 GPa), and amorphous Dvm (Figure 2 and Figure S5 in Supporting Information S1), consistent with XRD results (Figure 1). Notably, the grain size of Bgm strongly depends on the starting material: crystalline starting materials yield relatively coarse-grained products with a mean grain size of ~285 nm, providing the most reliable basis for compositional analysis, whereas glassy starting materials are associated with much finer grains with a mean grain size of ~65 nm (Figure S6 in Supporting Information S1), consistent with the weaker XRD reflections observed in

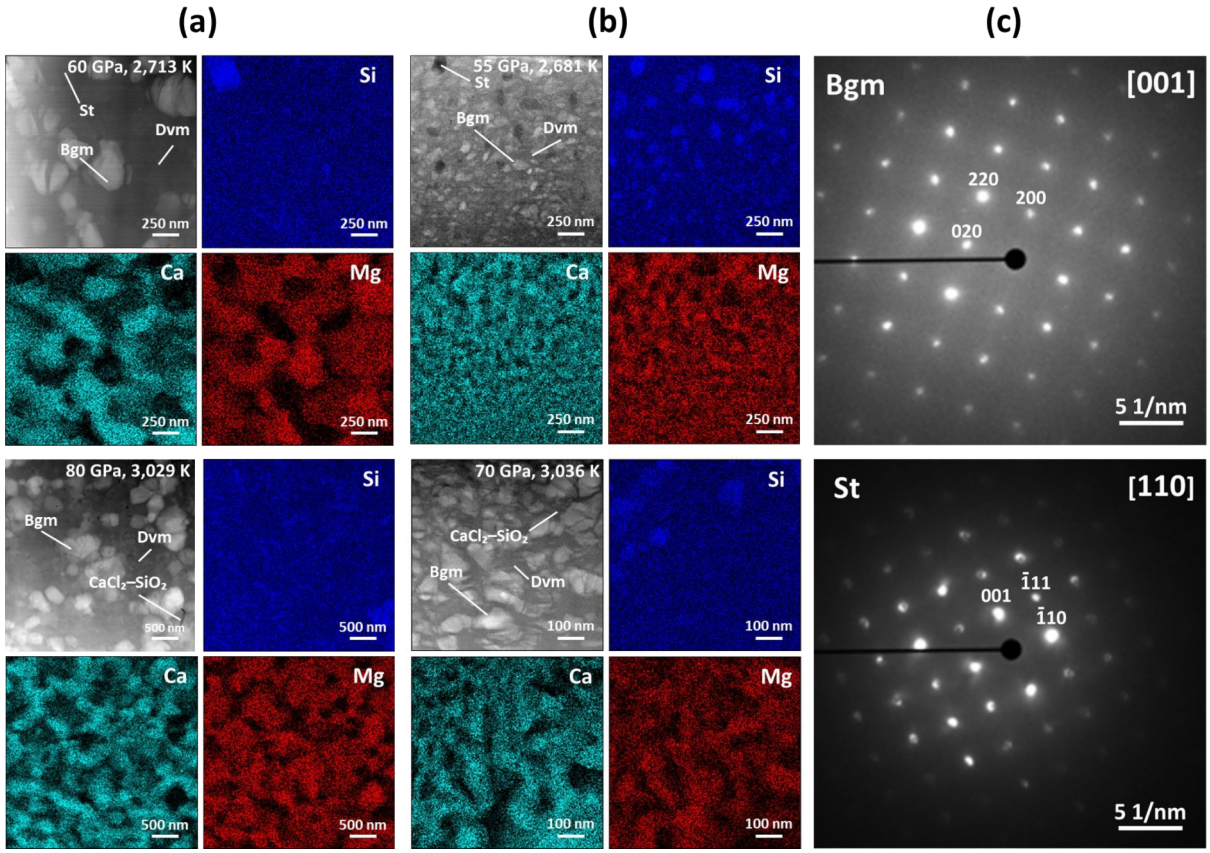

Figure 2. High-resolution transmission electron microscopy characterization of the recovered run products from high P-T experiments. For each panel set of four images in (a) and (b), dark-field transmission electron microscopy image is displayed at the top left together with energy-dispersive X-ray spectroscopy maps for Si (blue; top right), Ca (cyan; bottom left), and Mg (red; bottom right). The run products were quenched from high P-T using crystalline (a) and glass starting materials (b). The run products in (a) clearly displayed better crystalline features of the phases than that in (b). (c) Nano-beam electron diffraction patterns indexed to bridgmanite [001] and stishovite [110] with representative reflections labeled. Pressure and temperature conditions and scale bars for the syntheses are indicated within the panels.

the glass-derived runs. No systematic dependence of phase assemblage or χ_{Ca} on heating duration was observed, although longer heating of the glassy starting material could promote grain coarsening at relatively high temperatures. Bgm and St remained crystalline at ambient conditions, as confirmed by Nano-beam electron diffraction analysis (Figure 2c).

The χ_{Ca} in Bgm is determined to be 0.01–0.06 cations per formula unit at 55–124 GPa and 2,083–3,061 K (Table S1 in Supporting Information S1). Our measured χ_{Ca} in Bgm is consistent with the MAP results of Wang et al. (2025), in which the chemical equilibrium between Bgm and Dvm was achieved at conditions up to 50 GPa and 2,700 K with 24 hr annealing. Together with previous studies, our results suggest that the χ_{Ca} in Bgm is primarily controlled by temperature. An increase in temperature from 2,083 to 2,713 K at 60 GPa results in an increase in χ_{Ca} of ~0.01 (±0.002). Within uncertainty, no pressure dependence of χ_{Ca} is noticeable. The high χ_{Ca} in bridgmanite (0.2 cations per formula unit) reported by Ko et al. (2022) was not observed in any of our P-T runs. Detailed discussion about chemical analysis, ferric iron ratio, and Mg-Fe-Al incorporation in Dvm (χ_{Ca} of Dvm <1) is in Text S4 in Supporting Information S1.

3.3. Thermodynamic Modeling of Calcium Solubility in Bgm

To understand the χ_{Ca} in Bgm at relevant lower-mantle P-T conditions and its influence on lower mantle mineralogy, we constructed a thermodynamic model using the asymmetric Margules equation to estimate the Ca content in Bgm at different P-T conditions by calculating the solvus (mixing temperature) of Bgm and Dvm at different pressures (Figure 3). The asymmetric Margules equation is commonly used to describe the mixing

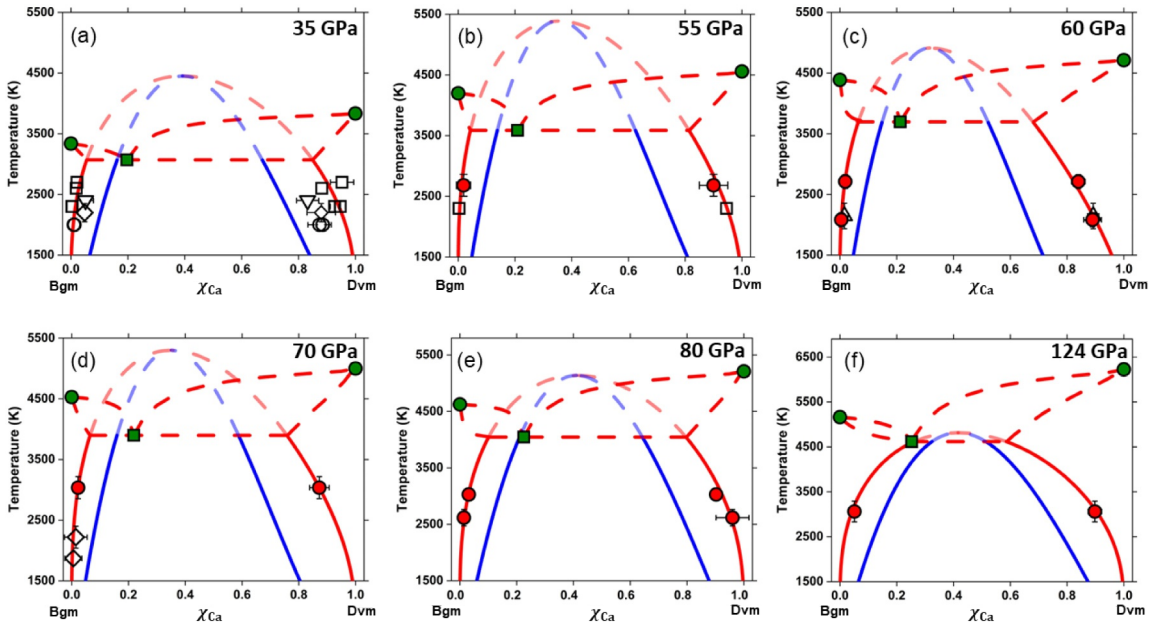

Figure 3. Temperature-dependent solvus in the bridgmanite–davemaoite system at high pressures. The solvus (red solid curve) and spinodal (blue solid curve) are grouped into six pressures at 35, 55, 60, 70, 80, and 124 GPa. χ_{Ca} denotes the mole fraction of the Ca component in bridgmanite or davemaoite, where $\chi_{Ca} = 0$ corresponds to Ca-free bridgmanite and $\chi_{Ca} = 1$ corresponds to davemaoite. Pale dashed curves indicate solvi and spinodal above the eutectic melting temperature. Red dashed curves are the calculated solidus and liquidus (Braithwaite & Stixrude, 2019). Solid red circles represent experimental data from this study. Open symbols denote literature data: downward triangles from Ricolleau et al. (2010), squares from Wang et al. (2025), circles from Ishii et al. (2022), upward triangles from Hirose et al. (2005), and diamonds for low χ_{Ca} Bgm from Ko et al. (2022). Green circles mark the melting temperatures of the endmember phases, and green squares denote the eutectic compositions (Braithwaite & Stixrude, 2019; Pierru et al., 2022; Zerr et al., 1997).

properties of minerals, such as feldspar (Eugster et al., 1972; Waldbaum & Thompson, 1969). The asymmetric Margules equation used in this study is as follows (White, 2020),

$$\Delta G^{\mathrm{mix}} = RT[x \ln x + (1-x)\ln(1-x)] + x(1-x)\,[W_{AB}(1-x) + W_{BA}x] \tag{1}$$

where ΔG^{mix} is the Gibbs free energy of mixing, x is the mole fraction of the Ca component, R is the gas constant, and T is temperature. W_{AB} and W_{BA} are the asymmetric Margules interaction parameters that describe the non-ideal mixing behavior on the Bgm and Dvm sides, respectively. The coexistence compositions of the two phases are denoted by x_1 and x_2, where x_1 is the Ca component content in the Bgm phase and x_2 is the Ca component content in the Dvm phase. These correspond to the two binodal compositions at a given pressure and temperature, with $x_1 < x_2$. The Margules parameters W_{AB} and W_{BA} were constrained by fitting the experimentally determined tie-line compositions, that is, the Ca contents in Bgm and Dvm, at their corresponding temperatures (x_1, x_2, T). For each experimental tie line, the coexistence compositions were required to satisfy the common-tangent condition applied to the Gibbs free-energy curve, which is equivalent to (Prieto, 2009),

$$\left.\frac{\partial \Delta G^{\mathrm{mix}}}{\partial x}\right|_{x_1} = \left.\frac{\partial \Delta G^{\mathrm{mix}}}{\partial x}\right|_{x_2} = \frac{\Delta G^{\mathrm{mix}}(x_2) - \Delta G^{\mathrm{mix}}(x_1)}{x_2 - x_1}. \tag{2}$$

The best-fit asymmetric Margules parameters, fitting statistics, and corresponding covariance matrices at each pressure are summarized in Tables S2 and S3 in Supporting Information S1. The spinodal was determined from the condition,

$$\frac{\partial^2 \Delta G^{\mathrm{mix}}}{\partial x^2} = 0. \tag{3}$$

We used Ca-free Bgm ($\chi_{Ca} = 0$) and pure $CaSiO_3$ Dvm ($\chi_{Ca} = 1$) as endmembers. The model was then used to calculate Bgm–Dvm solvi at different pressures. At 35 GPa, the fit is constrained by 8 tie lines, corresponding to 16 compositional data points from previous studies, providing a test of the applicability of the asymmetric Margules model (Figure 3a). In addition to "Ca-Bgm", Ko et al. (2022) also reported Bgm with low χ_{Ca} in separate runs, possibly due to larger grain sizes resulting from prolonged heating. Our solvus model can also accurately represent the low χ_{Ca} Bgm data reported by Ko et al. (2022) and the compositional data of Bgm and Dvm reported from studies using basaltic and Fe–Al-rich starting materials (Hirose et al., 2005; Ishii et al., 2022; Ricolleau et al., 2010; Wang et al., 2025) (Figure 3). Additional details of the thermodynamic framework and modeling procedure are provided in Text S5 in Supporting Information S1.

Our modeling results show that χ_{Ca} in Bgm increases strongly with temperature at a given pressure, while pressure effects are comparatively minor. The modeled temperature dependence of χ_{Ca} is on the order of 10^{-5} K^{-1}, over the relevant pressure range. Our calculated solvus and P-T dependence of χ_{Ca} are consistent with recent MAP data reported by Wang et al. (2025) (Figure 3b). Given the modeled P–T dependence and the persistently low χ_{Ca} up to 124 GPa and 3,061 K, we infer that the true mixing temperature must be substantially higher than 2,300 K. The constant mixing temperature of ~2,300 K for Bgm–Dvm proposed by Ko et al. (2022) is inconsistent with our findings.

4. Lower-Mantle Mineralogical and Geophysical Implications

Our experimental results, together with thermodynamic modeling, demonstrate that Ca has limited solubility in Bgm. The combined XRD and HRTEM results suggest that Dvm does not completely dissolve into Bgm at relevant lower-mantle P-T conditions. Instead, the disappearance of Dvm XRD peaks in runs using glass starting materials is likely attributable to kinetic factors, such as fine grain size from multiple nucleation centers and poor Dvm crystallinity. This finding is consistent with the results of Wang et al. (2025), suggesting that the previously reported "Ca-Bgm" by Ko et al. (2022) likely represents nanocrystalline phases or overestimated Ca contents resulting from small grain sizes. Similar kinetic effects in experiments using glass starting materials have been observed in previous studies, where metastable phases and nanocrystals of silicates were produced (Asahara et al., 2005; Irifune et al., 2016).

Taking the Ca solubility from our thermodynamic modeling into consideration, the mineralogical proportions of Bgm and Dvm in basaltic and pyrolitic models can be better constrained along representative lower-mantle geotherms (Katsura, 2022; Spiliopoulos & Stacey, 1984). To calculate χ_{Ca} in Bgm and the corresponding Dvm abundance along these geotherms, we used a two-stage pressure parameterization of the asymmetric Margules parameters. The best-fit W_{AB} and W_{BA} values used to construct the solvi in Figure 3 were obtained from the Bgm–Dvm tie-line compositions and were then fitted with linear functions of pressure. The limited and weakly pressure-dependent χ_{Ca} suggests a slight reduction in Dvm and a corresponding increase in Bgm in the deeper lower mantle. The strong temperature dependence of χ_{Ca} further implies a more pronounced reduction of Dvm in hotter regions of the lower mantle, such as near mantle plumes and the core–mantle boundary (CMB) (Figure 4). Details of the linear pressure parameterization are provided in Text S5 in Supporting Information S1. The results of our modeling indicate that Ca solubility in Bgm is as low as ~0.001 at topmost lower-mantle conditions; however, this value is extrapolated beyond the experimental temperature range and is therefore less well constrained than the higher P-T results. At ~115 GPa, χ_{Ca} reaches ~0.004, 0.013, and 0.03 along representative cold, normal, and hot geotherms, respectively. The Dvm fraction remains nearly constant for both pyrolite and MORB along the cold geotherm. Along the normal geotherm, Dvm abundance decreases only modestly with depth, by ~0.7% in pyrolite and ~0.3% in MORB, whereas along the hot geotherm both assemblages show a more pronounced decline in Dvm abundance. Overall, our model supports the traditional view that Dvm remains an abundant phase in lower-mantle mineralogy, with broadly maintained abundances of ~8 vol% in pyrolite and ~25 vol% in MORB (Irifune et al., 2010; Ishii et al., 2018, 2019, 2022; Kesson et al., 1998; Ricolleau et al., 2009, 2010), although stronger Dvm reduction may occur in hotter regions.

Dvm thus remains a major component in subducted MORB and pyrolitic assemblages in the lower mantle and is characterized by a distinctly low shear-wave velocity (Gréaux et al., 2019; Sun et al., 2016, 2022; Thomson et al., 2019; Zhou et al., 2025). We used Mie–Grüneisen EOS and finite-strain theory to evaluate how the modeled Dvm reduction affects density (ρ), bulk modulus (K_T), and bulk sound velocity (V_ϕ) in pyrolite and MORB (Ita & Stixrude, 1992; Stixrude & Lithgow-Bertelloni, 2005) (Figure S7 and Table S4 in Supporting Information S1).

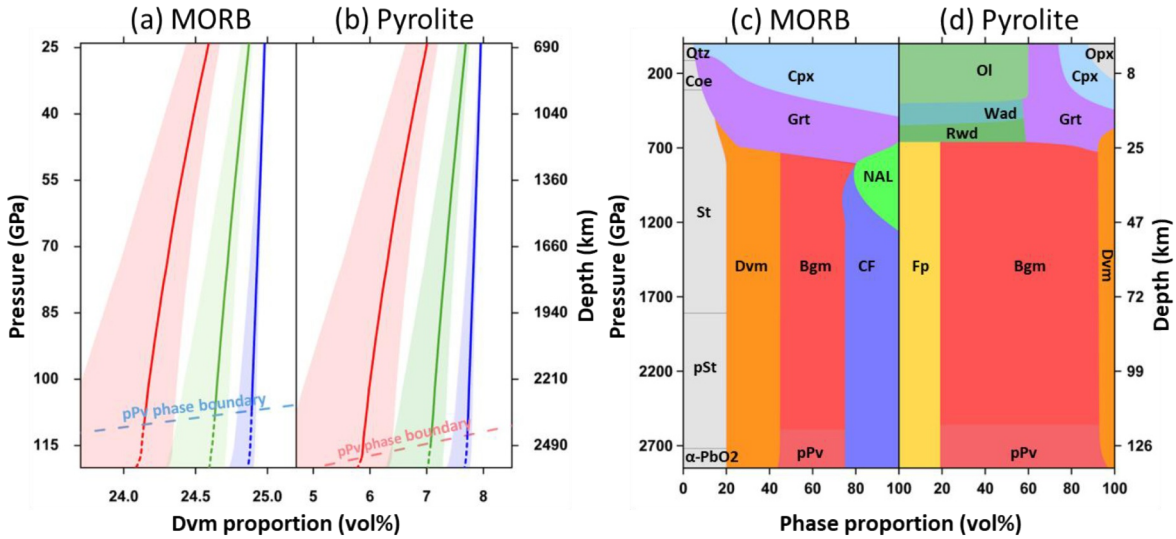

Figure 4. Davemaoite volume proportion and representative mineralogical diagrams of subducted mid-ocean ridge basalt (MORB) and pyrolite in the lower mantle. (a), (b) Calculated davemaoite volume proportion along representative cold (blue), normal (green), and hot (red) geotherms (Katsura, 2022; Spiliopoulos & Stacey, 1984) for MORB (a) and pyrolite (b). Shaded bands denote representative uncertainty ranges associated with the thermodynamic model. Dashed lines show extrapolated davemaoite fractions beyond the bridgmanite-to-post-perovskite transition, assuming that our thermodynamically modeled Ca solubility in bridgmanite can also be applied to post-perovskite. The red and blue dashed lines are the post-perovskite phase boundary for pyrolite and subducted basalt, respectively (Ohta et al., 2008). (c), (d) Mineralogical diagrams of MORB (c) and pyrolite (d) with depth in the lower mantle. The mineralogical diagrams follow previous studies, except that the bridgmanite–davemaoite boundary was modified according to the Ca-solubility model developed in this study (Ishii et al., 2022; Lin et al., 2013; Ricolleau et al., 2010; Stixrude & Lithgow-Bertelloni, 2012). Abbreviations: MORB, mid-ocean ridge basalt; Qtz, quartz; Coe, coesite; Cpx, clinopyroxene; Opx, orthopyroxene; Grt, garnet; Ol, olivine; Wad, wadsleyite; Rwd, ringwoodite; NAL, new-hexagonal aluminous phase; St, stishovite; Dvm, davemaoite; Bgm, bridgmanite; CF, Ca-ferrite-type phase; Fp, ferropericlase; pSt, post-stishovite ($CaCl_2$–type SiO_2); pPv, post-perovskite; α-PbO_2, α-PbO_2-type SiO_2.

The calculated changes are small, with slight increases in ρ and K_T and a slight decrease in V_ϕ, reflecting the limited Dvm reduction predicted by the solvus model. The maximum changes are $\Delta\rho \approx +0.27\%$, $\Delta K_T \approx +0.13\%$, and $\Delta V_\phi \approx -0.31\%$ for pyrolite, and $\Delta\rho \approx +0.19\%$, $\Delta K_T \approx +0.09\%$, and $\Delta V_\phi \approx -0.16\%$ for MORB. Consequently, these changes fall below typical seismic detectability and are unlikely to be resolved by current global tomography. Subducted MORB is expected to accumulate above the CMB, while much of it stagnates and mixes with the ambient lower mantle (Li & McNamara, 2013; Nakagawa et al., 2010; Xu et al., 2008). Interaction with the surrounding mantle and rising hot plumes may raise temperatures sufficiently for Bgm in the surrounding mantle to dissolve Dvm in subducted MORB. These processes can markedly decrease the Dvm proportion in subducted MORB in the lower mantle. To explore this endmember scenario of stronger Dvm reduction, we calculated the seismic properties of subducted MORB with progressively lower Dvm abundance. The results show that reduced Dvm increases V_P and V_S while leaving density nearly unchanged (Figure S8 and Text S6 in Supporting Information S1). This effect may help explain the discrepancy between high- and low-velocity anomalies attributed to subducted MORB in the lower mantle (Gréaux et al., 2019; Kaneshima, 2019, 2023; Thomson et al., 2019; Wang et al., 2020). Overall, Dvm is expected to persist in the lower mantle, but temperature-driven changes in its abundance can modify the seismic expression of recycled basaltic crust.

Conflict of Interest

The authors declare no conflicts of interest relevant to this study.

Availability Statement

The data used in this paper are available on Zenodo (C. Zhang, 2025) (from https://doi.org/10.5281/zenodo.18271026).

Acknowledgments
The authors thank C. Sun for his helpful discussion on thermodynamic modeling, S. K. Lee for assistance with sample synthesis, X. Zhan for assistance with TEM analysis, and F.-C. Sheu and I. Gearba for assistance with FIB sample preparation. We acknowledge the use of beamline 13-ID-D at GSECARS for the XRD experiments. GeoSoilEnviroCARS is supported by the National Science Foundation-Earth Sciences via SEES: Synchrotron Earth and Environmental Science (EAR-2223273). This research was performed on APS beam time awards (DOI: https://doi.org/10.46936/APS-188495/60013098, https://doi.org/10.46936/APS-188494/60013097, and https://doi.org/10.46936/APS-191650/60015353) from the Advanced Photon Source, a U.S. Department of Energy (DOE) Office of Science user facility operated for the DOE Office of Science by Argonne National Laboratory under Contract No. DE-AC02-06CH11357. J. F. L. acknowledges support from the Geophysics Program of the National Science Foundation of the United States (EAR-2333879). This crystalline sample synthesis was performed using the Joint-Use Facilities of the Institute for Planetary Materials, Okayama University.

References

Andrault, D., Bolfan-Casanova, N., & Guignot, N. (2001). Equation of state of lower mantle (Al, Fe)-MgSiO3 perovskite. *Earth and Planetary Science Letters*, *193*(3–4), 501–508. https://doi.org/10.1016/s0012-821x(01)00506-4

Asahara, Y., Ohtani, E., Kondo, T., Kubo, T., Miyajima, N., Nagase, T., et al. (2005). Formation of metastable cubic-perovskite in high-pressure phase transformation of Ca (Mg, Fe, Al) Si2O6. *American Mineralogist*, *90*(2–3), 457–462. https://doi.org/10.2138/am.2005.1649

Braithwaite, J., & Stixrude, L. (2019). Melting of CaSiO3 perovskite at high pressure. *Geophysical Research Letters*, *46*(4), 2037–2044. https://doi.org/10.1029/2018GL081805

Catalli, K., Shim, S.-H., Dera, P., Prakapenka, V. B., Zhao, J., Sturhahn, W., et al. (2011). Effects of the Fe3+ spin transition on the properties of aluminous perovskite—New insights for lower-mantle seismic heterogeneities. *Earth and Planetary Science Letters*, *310*(3–4), 293–302. https://doi.org/10.1016/j.epsl.2011.08.018

Criniti, G., Boffa Ballaran, T., Kurnosov, A., Liu, Z., Glazyrin, K., Merlini, M., et al. (2024). Thermal equation of state and structural evolution of Al-bearing bridgmanite. *Journal of Geophysical Research: Solid Earth*, *129*(1), e2023JB026879. https://doi.org/10.1029/2023JB026879

Eugster, H., Albee, A., Bence, A., Thompson, J., Jr., & Waldbaum, D. (1972). The two-phase region and excess mixing properties of paragonite-muscovite crystalline solutions. *Journal of Petrology*, *13*(1), 147–179. https://doi.org/10.1093/petrology/13.1.147

Gréaux, S., Irifune, T., Higo, Y., Tange, Y., Arimoto, T., Liu, Z., & Yamada, A. (2019). Sound velocity of CaSiO3 perovskite suggests the presence of basaltic crust in the Earth's lower mantle. *Nature*, *565*(7738), 218–221. https://doi.org/10.1038/s41586-018-0816-5

Hirose, K., Takafuji, N., Sata, N., & Ohishi, Y. (2005). Phase transition and density of subducted MORB crust in the lower mantle. *Earth and Planetary Science Letters*, *237*(1–2), 239–251. https://doi.org/10.1016/j.epsl.2005.06.035

Immoor, J., Miyagi, L., Liermann, H.-P., Speziale, S., Schulze, K., Buchen, J., et al. (2022). Weak cubic CaSiO3 perovskite in the Earth's mantle. *Nature*, *603*(7900), 276–279. https://doi.org/10.1038/s41586-021-04378-2

Irifune, T., Kawakami, K., Arimoto, T., Ohfuji, H., Kunimoto, T., & Shinmei, T. (2016). Pressure-induced nano-crystallization of silicate garnets from glass. *Nature Communications*, *7*(1), 13753. https://doi.org/10.1038/ncomms13753

Irifune, T., Shinmei, T., McCammon, C. A., Miyajima, N., Rubie, D. C., & Frost, D. J. (2010). Iron partitioning and density changes of pyrolite in Earth's lower mantle. *Science*, *327*(5962), 193–195. https://doi.org/10.1126/science.1181443

Ishii, T., Kojitani, H., & Akaogi, M. (2018). Phase relations and mineral chemistry in pyrolitic mantle at 1600–2200°C under pressures up to the uppermost lower mantle: Phase transitions around the 660-km discontinuity and dynamics of upwelling hot plumes. *Physics of the Earth and Planetary Interiors*, *274*, 127–137. https://doi.org/10.1016/j.pepi.2017.10.005

Ishii, T., Kojitani, H., & Akaogi, M. (2019). Phase relations of harzburgite and MORB up to the uppermost lower mantle conditions: Precise comparison with pyrolite by multisample cell high-pressure experiments with implication to dynamics of subducted slabs. *Journal of Geophysical Research: Solid Earth*, *124*(4), 3491–3507. https://doi.org/10.1029/2018JB016749

Ishii, T., Miyajima, N., Criniti, G., Hu, Q., Glazyrin, K., & Katsura, T. (2022). High pressure-temperature phase relations of basaltic crust up to mid-mantle conditions. *Earth and Planetary Science Letters*, *584*, 117472. https://doi.org/10.1016/j.epsl.2022.117472

Ita, J., & Stixrude, L. (1992). Petrology, elasticity, and composition of the mantle transition zone. *Journal of Geophysical Research*, *97*(B5), 6849–6866. https://doi.org/10.1029/92JB00068

Kaneshima, S. (2019). Seismic scatterers in the lower mantle near subduction zones. *Geophysical Journal International*, *219*(Supplement_1), S2–S20. https://doi.org/10.1093/gji/ggz241

Kaneshima, S. (2023). Mid-mantle seismic scatterers beneath the Samoan hotspot. *Physics of the Earth and Planetary Interiors*, *340*, 107034. https://doi.org/10.1016/j.pepi.2023.107034

Katsura, T. (2022). A revised adiabatic temperature profile for the mantle. *Journal of Geophysical Research: Solid Earth*, *127*(2), e2021JB023562. https://doi.org/10.1029/2021JB023562

Kesson, S., Fitz Gerald, J., & Shelley, J. (1998). Mineralogy and dynamics of a pyrolite lower mantle. *Nature*, *393*(6682), 252–255. https://doi.org/10.1038/30466

Ko, B., Greenberg, E., Prakapenka, V., Alp, E. E., Bi, W., Meng, Y., et al. (2022). Calcium dissolution in bridgmanite in the Earth's deep mantle. *Nature*, *611*(7934), 88–92. https://doi.org/10.1038/s41586-022-05237-4

Li, M., & McNamara, A. K. (2013). The difficulty for subducted oceanic crust to accumulate at the Earth's core-mantle boundary. *Journal of Geophysical Research: Solid Earth*, *118*(4), 1807–1816. https://doi.org/10.1002/jgrb.50156

Lin, J. F., Speziale, S., Mao, Z., & Marquardt, H. (2013). Effects of the electronic spin transitions of iron in lower mantle minerals: Implications for deep mantle geophysics and geochemistry. *Reviews of Geophysics*, *51*(2), 244–275. https://doi.org/10.1002/rog.20010

McDonough, W. F., & Sun, S.-S. (1995). The composition of the Earth. *Chemical Geology*, *120*(3–4), 223–253. https://doi.org/10.1016/0009-2541(94)00140-4

Muir, J. M., Thomson, A. R., & Zhang, F. (2021). The miscibility of calcium silicate perovskite and bridgmanite: A single perovskite solid solution in hot, iron-rich regions. *Earth and Planetary Science Letters*, *566*, 116973. https://doi.org/10.1016/j.epsl.2021.116973

Muir, J. M., & Zhang, F. (2022). The effect of Ti on Ca-pv and Mg-pv phase stability. *Physics of the Earth and Planetary Interiors*, *322*, 106825. https://doi.org/10.1016/j.pepi.2021.106825

Nakagawa, T., Tackley, P. J., Deschamps, F., & Connolly, J. A. (2010). The influence of MORB and harzburgite composition on thermo-chemical mantle convection in a 3-D spherical shell with self-consistently calculated mineral physics. *Earth and Planetary Science Letters*, *296*(3–4), 403–412. https://doi.org/10.1016/j.epsl.2010.05.026

Ohta, K., Hirose, K., Lay, T., Sata, N., & Ohishi, Y. (2008). Phase transitions in pyrolite and MORB at lowermost mantle conditions: Implications for a MORB-rich pile above the core–mantle boundary. *Earth and Planetary Science Letters*, *267*(1–2), 107–117. https://doi.org/10.1016/j.epsl.2007.11.037

Pierru, R., Pison, L., Mathieu, A., Gardés, E., Garbarino, G., Mezouar, M., et al. (2022). Solidus melting of pyrolite and bridgmanite: Implication for the thermochemical state of the Earth's interior. *Earth and Planetary Science Letters*, *595*, 117770. https://doi.org/10.1016/j.epsl.2022.117770

Prakapenka, V., Kubo, A., Kuznetsov, A., Laskin, A., Shkurikhin, O., Dera, P., et al. (2008). Advanced flat top laser heating system for high pressure research at GSECARS: Application to the melting behavior of germanium. *High Pressure Research*, *28*(3), 225–235. https://doi.org/10.1080/08957950802050718

Prieto, M. (2009). Thermodynamics of solid solution-aqueous solution systems. *Reviews in Mineralogy and Geochemistry*, *70*(1), 47–85. https://doi.org/10.2138/rmg.2009.70.2

Ricolleau, A., Fei, Y., Cottrell, E., Watson, H., Deng, L., Zhang, L., et al. (2009). Density profile of pyrolite under the lower mantle conditions. *Geophysical Research Letters*, *36*(6), L06302. https://doi.org/10.1029/2008GL036759

Ricolleau, A., Perrillat, J. P., Fiquet, G., Daniel, I., Matas, J., Addad, A., et al. (2010). Phase relations and equation of state of a natural MORB: Implications for the density profile of subducted oceanic crust in the Earth's lower mantle. *Journal of Geophysical Research*, *115*(B8). https://doi.org/10.1029/2009JB006709

Ringwood, A., & Irifune, T. (1988). Nature of the 650–km seismic discontinuity: Implications for mantle dynamics and differentiation. *Nature*, *331*(6152), 131–136. https://doi.org/10.1038/331131a0

Ringwood, A. E. (1991). Phase transformations and their bearing on the constitution and dynamics of the mantle. *Geochimica et Cosmochimica Acta*, *55*(8), 2083–2110. https://doi.org/10.1016/0016-7037(91)90090-r

Spiliopoulos, S., & Stacey, F. (1984). The Earth's thermal profile: Is there a mid-mantle thermal boundary layer? *Journal of Geodynamics*, *1*(1), 61–77. https://doi.org/10.1016/0264-3707(84)90006-1

Stixrude, L., & Lithgow-Bertelloni, C. (2005). Thermodynamics of mantle minerals—I. Physical properties. *Geophysical Journal International*, *162*(2), 610–632. https://doi.org/10.1111/j.1365-246x.2005.02642.x

Stixrude, L., & Lithgow-Bertelloni, C. (2012). Geophysics of chemical heterogeneity in the mantle. *Annual Review of Earth and Planetary Sciences*, *40*(1), 569–595. https://doi.org/10.1146/annurev.earth.36.031207.124244

Sun, N., Bian, H., Zhang, Y., Lin, J.-F., Prakapenka, V. B., & Mao, Z. (2022). High-pressure experimental study of tetragonal CaSiO3-perovskite to 200 GPa. *American Mineralogist*, *107*(1), 110–115. https://doi.org/10.2138/am-2021-7913

Sun, N., Mao, Z., Yan, S., Wu, X., Prakapenka, V. B., & Lin, J. F. (2016). Confirming a pyrolitic lower mantle using self-consistent pressure scales and new constraints on CaSiO3 perovskite. *Journal of Geophysical Research: Solid Earth*, *121*(7), 4876–4894. https://doi.org/10.1002/2016JB013062

Sun, N., Shi, W., Mao, Z., Zhou, C., & Prakapenka, V. B. (2019). High pressure-temperature study on the thermal equations of state of seifertite and CaCl2-type SiO2. *Journal of Geophysical Research: Solid Earth*, *124*(12), 12620–12630. https://doi.org/10.1029/2019JB017853

Tange, Y., Kuwayama, Y., Irifune, T., Funakoshi, K. i., & Ohishi, Y. (2012). P-V-T equation of state of MgSiO3 perovskite based on the MgO pressure scale: A comprehensive reference for mineralogy of the lower mantle. *Journal of Geophysical Research*, *117*(B6). https://doi.org/10.1029/2011JB008988

Thomson, A., Crichton, W., Brodholt, J., Wood, I., Siersch, N., Muir, J., et al. (2019). Seismic velocities of CaSiO3 perovskite can explain LLSVPs in Earth's lower mantle. *Nature*, *572*(7771), 643–647. https://doi.org/10.1038/s41586-019-1483-x

van Aken, P. A., & Liebscher, B. (2002). Quantification of ferrous/ferric ratios in minerals: New evaluation schemes of Fe L2,3 electron energy-loss near-edge spectra. *Physics and Chemistry of Minerals*, *29*(3), 188–200. https://doi.org/10.1007/s00269-001-0222-6

Waldbaum, D., & Thompson, J., Jr. (1969). Mixing properties of sanidine crystalline solutions: IV. Phase diagrams from equations of state. *American Mineralogist*, *54*(9–10), 1274–1298.

Wang, L., Miyajima, N., Wang, F., & Katsura, T. (2025). Persistence of davemaoite at lower-mantle conditions. *Nature Geoscience*, *18*(4), 365–369. https://doi.org/10.1038/s41561-025-01657-9

Wang, W., Xu, Y., Sun, D., Ni, S., Wentzcovitch, R., & Wu, Z. (2020). Velocity and density characteristics of subducted oceanic crust and the origin of lower-mantle heterogeneities. *Nature Communications*, *11*(1), 64. https://doi.org/10.1038/s41467-019-13720-2

White, W. M. (2020). *Geochemistry*. John Wiley and Sons.

Wolf, A. S., Jackson, J. M., Dera, P., & Prakapenka, V. B. (2015). The thermal equation of state of (Mg, Fe) SiO3 bridgmanite (perovskite) and implications for lower mantle structures. *Journal of Geophysical Research: Solid Earth*, *120*(11), 7460–7489. https://doi.org/10.1002/2015JB012108

Xu, W., Lithgow-Bertelloni, C., Stixrude, L., & Ritsema, J. (2008). The effect of bulk composition and temperature on mantle seismic structure. *Earth and Planetary Science Letters*, *275*(1–2), 70–79. https://doi.org/10.1016/j.epsl.2008.08.012

Zerr, A., Serghiou, G., & Boehler, R. (1997). Melting of CaSiO3 perovskite to 430 kbar and first in-situ measurements of lower mantle eutectic temperatures. *Geophysical Research Letters*, *24*(8), 909–912. https://doi.org/10.1029/97GL00829

Zhang, C. (2025). Dataset of "Calcium Solubility of Bridgmanite in Subducted Basalt in Earth's Lower Mantle" [Dataset]. *Zenodo*. https://doi.org/10.5281/zenodo.18271026

Zhou, W.-Y., Hao, M., Su, W., Kim, T., Chen, S., Shim, S.-H., et al. (2025). Elasticity of davemaoite as a primary contributor to lower-mantle heterogeneities. *Science*, *390*(6776), 935–939. https://doi.org/10.1126/science.adx8356

References From the Supporting Information

Chidester, B., Thompson, E., Fischer, R., Heinz, D., Prakapenka, V., Meng, Y., & Campbell, A. (2021). Experimental thermal equation of state of B2-KCl. *Physical Review B*, *104*(9), 094107. https://doi.org/10.1103/PhysRevB.104.094107

Fei, Y., Ricolleau, A., Frank, M., Mibe, K., Shen, G., & Prakapenka, V. (2007). Toward an internally consistent pressure scale. *Proceedings of the National Academy of Sciences*, *104*(22), 9182–9186. https://doi.org/10.1073/pnas.0609013104

Fei, H., Faul, U., & Katsura, T. (2021). The grain growth kinetics of bridgmanite at the topmost lower mantle. *Earth and Planetary Science Letters*, *561*, 116820. https://doi.org/10.1016/j.epsl.2021.116820

Fei, H., Ballmer, M. D., Faul, U., Walte, N., Cao, W., & Katsura, T. (2023). Variation in bridgmanite grain size accounts for the mid-mantle viscosity jump. *Nature*, *620*(7975), 794–799. https://doi.org/10.1038/s41586-023-06215-0

Frost, D. J., Liebske, C., Langenhorst, F., McCammon, C. A., Trønnes, R. G., & Rubie, D. C. (2004). Experimental evidence for the existence of iron-rich metal in the Earth's lower mantle. *Nature*, *428*(6981), 409–412. https://doi.org/10.1038/nature02413

Fu, S., Yang, J., Zhang, Y., Liu, J., Greenberg, E., Prakapenka, V. B., et al. (2018). Melting behavior of the lower-mantle ferropericlase across the spin crossover: Implication for the ultra-low velocity zones at the lowermost mantle. *Earth and Planetary Science Letters*, *503*, 1–9. https://doi.org/10.1016/j.epsl.2018.09.014

Hill, R. (1952). The elastic behaviour of a crystalline aggregate. *Proceedings of the Physical Society Section A*, *65*(5), 349–354. https://doi.org/10.1088/0370-1298/65/5/307

Kim, H.-I., & Lee, S. K. (2019). The degree of polymerization and structural disorder in (Mg, Fe) SiO3 glasses and melts: Insights from high-resolution 29Si and 17O solid-state NMR. *Geochimica et Cosmochimica Acta*, *250*, 268–291. https://doi.org/10.1016/j.gca.2019.02.018

Koningsveld, R., Stockmayer, W. H., & Nies, E. (2001). *Polymer phase diagrams: A textbook*. Oxford University Press.

Lee, S. K., Mosenfelder, J. L., Park, S. Y., Lee, A. C., & Asimow, P. D. (2020). Configurational entropy of basaltic melts in Earth's mantle. *Proceedings of the National Academy of Sciences*, *117*(36), 21938–21944. https://doi.org/10.1073/pnas.2014519117

Nomura, R., Zhou, Y., & Irifune, T. (2017). Melting phase relations in the MgSiO3–CaSiO3 system at 24 GPa. *Progress in Earth and Planetary Science*, *4*, 1–11. https://doi.org/10.1186/s40645-017-0149-2

Prescher, C., & Prakapenka, V. B. (2015). DIOPTAS: A program for reduction of two-dimensional X-ray diffraction data and data exploration. *High Pressure Research*, *35*(3), 223–230. https://doi.org/10.1080/08957959.2015.1059835

Sinmyo, R., & Hirose, K. (2010). The Soret diffusion in laser-heated diamond-anvil cell. *Physics of the Earth and Planetary Interiors*, *180*(3–4), 172–178. https://doi.org/10.1016/j.pepi.2009.10.011

Stixrude, L., & Lithgow-Bertelloni, C. (2024). Thermodynamics of mantle minerals–III: The role of iron. *Geophysical Journal International*, *237*(3), 1699–1733. https://doi.org/10.1093/gji/ggae126

Toby, B. H., & Von Dreele, R. B. (2013). GSAS-II: The genesis of a modern open-source all purpose crystallography software package. *Journal of Applied Crystallography*, *46*(2), 544–549. https://doi.org/10.1107/S0021889813003531

Zhang, Y., Fu, S., Wang, B., & Lin, J.-F. (2021). Elasticity of a pseudoproper ferroelastic transition from stishovite to post-stishovite at high pressure. *Physical Review Letters*, *126*(2), 025701. https://doi.org/10.1103/physrevlett.126.025701